Materials Reports: Energy 5 (2025) 100378

Contents lists available at ScienceDirect

Materials Reports: Energy

journal homepage: www.keaipublishing.com/en/journals/materials-reports-energy

Original Research Report

Engineering of entropy-driven surface doping towards stabilized high-voltage NCM cathodes: Li (Ni, Co, Mn, Ce, La, Zr, Al) O_x

Leqi Zhao[a,b], Zezhou Lin[c], Yijun Zhong[a], Hanwen Liu[a], Xiao Sun[b], Yu-Cheng Huang[a], William D.A. Rickard[b], Tony Tang[d], Zongping Shao[a,*]

[a] Curtin Centre for Advanced Energy Materials and Technologies, WA School of Mines: Minerals, Energy and Chemical Engineering (WASM-MECE), Curtin University, Perth, Western Australia, 6102, Australia
[b] John De Laeter Centre, Curtin University, Perth, WA 6102, Australia
[c] Department of Applied Physics, The Hong Kong Polytechnic University, 999077, China
[d] WA School of Mines: Minerals, Energy and Chemical Engineering (WASM-MECE), Curtin University, Perth, WA 6102, Australia

ARTICLE INFO

Keywords:
Lithium-ion battery
NCM811 cathode modification
High-entropy surface doping
High-voltage stability

ABSTRACT

Ni-rich $LiNi_{0.8}Mn_{0.1}Co_{0.1}O_2$ (NCM) cathodes in layered oxide cathodes are attractive for high-energy lithium-ion batteries but suffer from rapid capacity fade and thermal instability at high charge voltages. In this study, we propose an entropy-assisted multi-element doping strategy to mitigate these issues. Specifically, two routes are designed and compared: bulk-like localized high-entropy doping (BHE-NCM) and surface-distributed high-entropy-zone doping (SHE-NCM). The surface entropy-doped NCM cathode delivers enhanced electrochemical performance, including higher capacity retention under 4.5 V cycling and superior rate capability, compared to both bulk-like and pristine counterparts. Comprehensive material characterization reveals that surface-localized doping stabilizes the layered structure with reduced microcrack formation and creates a uniform dopant-rich surface region with improved thermal and electrochemical stability. Overall, entropy-assisted doping at the near surface zone effectively alleviates structural degradation and interface reactions in Ni-rich NCM, enabling improved cycling performance at high voltage. This work highlights the significance of surface entropy engineering as a promising strategy for designing high-voltage cathodes with improved safety and longevity.

1. Introduction

Lithium-ion batteries (LIBs) are essential for applications ranging from consumer electronics to electric vehicles, owing to their high energy density and long cycle life. Ni-rich $LiNi_{0.8}Mn_{0.1}Co_{0.1}O_2$ (NCM811) cathodes are promising for next-generation LIBs due to their high capacity and reduced cobalt content, driven by the multiple redox states of Ni.[1] However, this increased nickel content also introduces vulnerabilities, including Li/Ni cation mixing due to similar ionic radii, phase transitions during cycling, and lattice oxygen loss, particularly during the H2-H3 transformation.[2] Traditional stabilization mechanisms, including surface coating[3,4] and extrinsic ion doping,[5,6] while effective in low-nickel NCM (e.g., NCM111) or medium-nickel NCM (e.g., NCM523) cathodes at standard voltage, prove inadequate for nickel-rich NCM (Ni $\geq$ 80%) cathodes at higher voltage due to the oxygen evolution-induced structural degradation. This underscores the need for innovative approaches to enhance the performance and stability of high-voltage NCM cathodes.

High-entropy design is a recent and innovative approach to cathode material modification. This strategy leverages the unique characteristics of high-entropy materials, traditionally utilized in catalytic systems for their superior stability and catalytic activity.[7] High-entropy materials possess beneficial attributes, including enhanced mechanical robustness, excellent corrosion resistance, adjustable functional properties, and superior thermal stability, all critical for improved cathode performance.[8] For instance, Fu et al.[9] employed configurational entropy and ion-diffusion structural tuning to modify sodium layered oxide cathodes, $NaMNO_2$ ($Na_{0.62}Mn_{0.67}Ni_{0.23}Cu_{0.05}Mg_{0.09-2y}Ti_yO_2$), achieving notable enhancements in electrochemical performance and stability by mitigating structural distortion and cationic rearrangement caused by irreversible phase transitions. Similarly, Zhang et al.[10] developed a high-entropy doped, high-nickel, cobalt-free layered oxide cathode

* Corresponding author.
E-mail address: zongping.shao@curtin.edu.au (Z. Shao).

Peer review under the responsibility of Editorial Office of Chongqing Xixin Tianyuan Data & Information Co., Ltd.

https://doi.org/10.1016/j.matre.2025.100378
Received 26 May 2025; Received in revised form 1 July 2025; Accepted 7 July 2025
Available online 16 October 2025

($LiNi_{0.8}Mn_{0.13}Ti_{0.02}Mg_{0.02}Nb_{0.01}Mo_{0.02}O_2$), demonstrating outstanding thermal and cycling stability. The cathode exhibited nearly zero volumetric change during cycling, effectively minimizing lattice defects and local strain-induced cracking. In-situ heating experiments further validated its enhanced thermal stability, comparable to that of the ultra-stable NMC-532 material.

A similar layered oxide material, $LiCoO_2$, with high-entropy modification was reported by Tan et al.[11] By co-doping with Mg, Al, Eu, Co, and Li, this material achieved enhanced structural integrity and electrochemical stability. The improvement stems from the formation of a high-entropy near-surface zone, featuring a disordered rock-salt shell and dopant-segregated surface, which effectively suppresses oxygen release and structural degradation. Moreover, the reversibility between the O3 and H1-3 phases and the cathode's thermal stability were significantly enhanced under a 4.6 V cut-off. This addresses a major challenge for all layered oxide materials (including NCM811), where higher charge voltages increase energy density of batteries but accelerate cathode degradation. In a related study, Zhao et al.[12] introduced ultra-high-Ni NCM9055 cathodes with epitaxial high-entropy surface coatings composed of Ni, Co, Mn, Nb, Zr, and W. Their entropy-assisted coating, formed through oriented attachment reactions between Wadsley-Roth oxides and layered NCM, offered superior resistance to cracking and corrosion along with enhanced ion transport. The coated cathodes exhibited improved fast-charging behavior, thermal stability, and durability across wide temperature ranges.

In this study, we propose a high-entropy doping approach utilizing Ce, La, Zr, and Al (CLZA) dopants to engineer a structurally robust and compositionally complex surface on high-nickel NCM cathode particles. This method leverages the intrinsic self-segregation behavior of these dopants, significantly enhancing the structural integrity and electrochemical stability of the cathode, particularly at high operating voltages. The selected high-entropy dopants each uniquely contribute to cathode stability. Zirconium doping facilitates lattice stabilization and alleviates the degree of cation mixing through robust Zr–O bonding interactions, benefiting from its similar ionic radius to lithium, i.e., Li^+ (0.76 Å) and Zr^{4+} (0.72 Å).[12–16] Although electrochemically inactive, rare-earth ions Ce^{3+} and La^{3+} occupy lithium lattice sites and strengthen neighbouring oxygen ions through robust ionic interactions, which effectively suppress oxygen oxidation and release, as demonstrated in experimental and theoretical studies.[13–18] Compared to Li, the larger ionic radii of Ce^{3+} (1.01 Å) and La^{3+} (1.03 Å) ions contribute to lattice stabilization by inducing lattice strain relaxation, thereby reducing the formation of lattice defects and cracks during cycling. Additionally, substituting Al at transition metal sites facilitates the formation of stronger Al–O bonds compared to typical transition metal-oxygen bonds, enhancing thermal and structural stability by mitigating lattice distortion and volume changes during cycling.[11,20–24]

To study how the compositional architecture of high-entropy doping influences structural evolution and electrochemical performance, two entropy-driven doping strategies were explored in this work, namely, bulk-like localized high-entropy doping (BHE-NCM) and surface-distributed high-entropy-zone doping (SHE-NCM). The BHE-NCM adopts a simultaneous high-temperature co-doping upon lithiation, whereas the SHE-NCM is designed with a stepwise and temperature-mediated doping strategy, a proven technique to spatially control the radial distribution of individual dopants based on their ionic radii and functional roles.[15,16,23,24] Structural stabilizers Al^{3+} and Zr^{4+} are introduced at higher temperatures after lithiation to enable moderate lattice incorporation near the particle surface, while larger rare-earth dopants Ce^{3+} and La^{3+} are applied via medium-temperature post-annealing to confine them to the outermost surface region and avoid the excessive bulk disorder. As a result, the engineered surface entropy zone facilitates reduced Ni/Li cation mix, suppressed oxygen evolution, minimized impedance growth, and eventually improves the electrochemical stability of the Ni-rich cathode under high-voltage operation.

2. Experimental methods

The synthesis of the NCM811 precursor is derived from earlier work.[25]

2.1. Preparation of bulk-like localized high-entropy doping

To achieve bulk-like localization of dopants, the NCM precursor was wet-mixed with 2 mol% of $Al(NO_3)_3{\cdot}9H_2O$ (99.99%), $ZrO(NO_3)_2$ (99.99%), $Ce(NO_3)_2{\cdot}6H_2O$ (99.99%), $La(NO_3)_3{\cdot}6H_2O$ (99.99%) using water and stirred at 700 rpm overnight. The resulting mixture was transferred into a Teflon-lined autoclave and subjected to hydrothermal treatment at 180 °C for 8 h. After cooling, the solid product was collected via centrifugation and dried under vacuum at 80 °C. Lithiation was then performed by mixing the modified NCM precursor with 10% $LiOH{\cdot}H_2O$ (99.95%, Sigma-Aldrich). A two-step calcination process was employed under flowing pure oxygen (50 mL min^{-1}): the first stage at 480 °C for 5 h facilitated the removal of residual organics and initial oxide formation; the second stage at 750 °C for 12 h promoted crystallization, enabling the development of uniform, localized and well-crystallized BHE-NCM particles.

2.2. Preparation of surface-doped NCM

The NCM precursor is directly lithiated with 10% $LiOH{\cdot}H_2O$ (99.95%, Sigma-Aldrich) and undergoes the two-stage calcination process under the same conditions aforementioned. The obtained NCM cathode is wet-mixed with 2 mol% of $Al(NO_3)_3{\cdot}9H_2O$ and $ZrO(NO_3)_2$ using isopropanol and stirred at 700 rpm overnight. The mixed solution is transferred to Teflon lined autoclave and heated to 180 °C for solvothermal treatment for 8 h. After drying, the sample is annealed at 700 °C for 3 h. This is followed by solvothermal treatment with 2 mol% of $Ce(NO_3)_2{\cdot}6H_2O$ and $La(NO_3)_3{\cdot}6H_2O$ at 160 °C for 8 h, and a second stage annealing performed at 500 °C for 3 h to obtain the final SHE-NCM particles.

2.3. Material characterization

The morphology of both as-synthesized cathodes and their post-cycled counterparts was directly visualized using a dual-beam focused ion beam scanning electron microscope (FIB-SEM, ZEISS NEON 40EsB). Additionally, X-ray diffraction (XRD) was employed to examine the crystal structure and compositional information of the catholyte interlayer before and after cycling. This analysis utilized a Bragg-Brentano geometry X-ray Diffractometer (Bruker D8A) with a copper X-ray source. The crystal structures of doped BHE-NCM and SHE-NCM were further analyzed using a transmission electron microscope (TEM, FEI Talos FS200X G2) equipped with a field emission gun (FEG). Interplanar spacings were measured using ImageJ software and cross-validated with X-ray diffraction (XRD) data. High-angle annular dark-field scanning transmission electron microscopy (HAADF-STEM) integrated with energy-dispersive X-ray spectroscopy (EDS) was used to map the elemental distribution at the edges of the NCM particles.

X-ray photoelectron spectroscopy (XPS) was utilized to analyze the chemical composition of the cathode electrode interlayer after galvanostatic cycling. The analysis was conducted using a Kratos Axis Ultra XPS instrument, with a hybrid lens and a monochromatic Al Kα (1486.6 eV) radiation source, operating at gun power of 150 W (15 kV, 10 mA). Two pass energies were selected: 160 eV for full (wide) spectra and 40 eV for high-resolution spectra. Depth profiling was performed using a 5 kV monoatomic Ar^+ ion source for the as-synthesized doped NCM (pressed into pellets for Ar^+ etching, with 10 etching cycles, 6 min each), and a 10 kV gas cluster ion source with cluster size of Ar^+_{500} for the cathode-electrolyte interphase (CEI) after electrochemical charge/discharge (5 etching cycles, 30 s each). The raw XPS spectra were analyzed using CasaXPS software, mathematically corrected and fitted

using Shirley background subtraction and calibrated to the C−C/C−H peak (284.8 eV) arising from adventitious carbon contamination. Time-of-flight secondary-ion mass spectrometry (TOF-SIMS) analysis was performed using IONTOF M6 ToF-SIMS with Bi^+ and Bi_3^+ ion source to study the spatial distribution of the post-cycled NCM cathode. X-ray absorption spectroscopy (XAS) experiments, including both X-ray absorption near-edge structure (XANES) and extended X-ray absorption fine structure (EXAFS), were performed in fluorescence mode at the Tender X-ray bending-magnet beamline TPS 32A (Tender X-ray absorption spectroscopy beamline) (1.7–10 keV) of the Taiwan Photon Source, National Synchrotron Radiation Research Center. A fly-scan acquisition scheme enabled the collection of complete XAFS spectra spanning >800 eV in under 15 s. For nickel analysis, Ni K-edge (8333 eV) XANES/EXAFS spectra were recorded with an energy resolution of ~0.40 eV, affording precise insight into the oxidation state and local coordination environment of Ni sites.

Simultaneous weight change (TGA) and true differential heat flow (DSC) data were recorded and analyzed using TA Instruments SDT Q600. Samples weighing less than 20 mg were heated in alumina crucibles from room temperature to 700 °C at a rate of 10 °C min^{-1} under a continuous nitrogen flow. Pfeiffer Prisma QMS 200 was employed to assess lattice oxygen release from charged NCM cathodes. The batteries were first electrochemically delithiated by charging to 4.5 V (vs. Li/Li^+) at 1C for 1 h, following a constant current-constant voltage (CC-CV) procedure. After reaching 80%–90% state-of-charge, the cathodes were retrieved, rinsed thoroughly with dimethyl carbonate (DMC) to remove residual electrolyte, and dried under an inert atmosphere. The dried cathode films were then introduced into the mass spectrometer (MS-Prisma QMS 200), and the mass charge ratio of oxygen ($m/z = 32$) was analyzed under a helium atmosphere from room temperature to 700 °C.

The ionization efficiency correction of Prisma QMS and Faraday's Law is used to derive the normalized gas release rate n (μmol min^{-1} g_{CAM}^{-1}), to quantitatively analyze the different extent of oxygen evolution in delithiated NCM cathodes,[26] as shown in Equation (1) below:

$$n = \left(\frac{I}{q \cdot \eta \cdot N_A \cdot m_{CAM}}\right) \quad (1)$$

Where I is the ion current (A). q is the elementary charge (1.6×10^{-19} C or 1.6×10^{-19} A s). η is the ionization efficiency correction (0.001). N_A is Avogadro's number (6.022×10^{23} mol^{-1}). m_{CAM} is the mass of cathode active material in mg.

2.4. Electrochemical characterization

The staircase potentiostatic electrochemical impedance spectroscopy (SPEIS) during cycling was determined electrochemically using a potentiostat BioLogic VSP and EC-lab in a Li-NCM half-cell. EIS measurements (100 mHz-200 kHz) were conducted at key voltage points (e.g., phase transition points) during 0.2C charge/discharge cycles. Stepwise cyclic voltammetry (CV) was performed at scanning rates of 0.1, 0.2, 0.3, 0.4, 0.5, 1.0, 2.0 and 3.0 mV s^{-1}, to validate the improved electrochemical stability of SHE-NCM. To assess the battery performance of the full cells, a LANHE battery test system was employed to conduct galvanostatic charge and discharge at a cut-off voltage of 4.3 and 4.5 V under a constant current density of 1C, which was calculated using the theoretical capacity of stoichiometric NCM811, i.e., 275.6 mAh g^{-1}.

The Randles-Sevcik equation[27,28] is used to evaluate the lithium diffusion coefficient D, as shown in Equation (2) below:

$$I_p = 2.69 \times 10^5 \, n^{3/2} A D^{1/2} C v^{1/2} \quad (2)$$

Where I_p is the current maximum in amperes (A). n is the number of electrons transferred in the redox event. A is the electrode area in cm^2. D is the diffusion coefficient in cm^2 s^{-1}. C is the concentration in mol cm^{-3}. v is the scan rate in V s^{-1}.

3. Results and discussion

3.1. Design principle and structure analysis of HE-NCM

High-entropy doping's structural impact was assessed via particle morphology and crystal structure characterization. The crystal structural differences between BHE-NCM and SHE-NCM were first evaluated through XRD analysis. Both doped samples maintained the characteristic layered hexagonal α-$NaFeO_2$ structure (space group R-3m),[6,9,29] with no significant peak shifts compared to pristine NCM811, indicating the preservation of the primary crystal framework. However, Fig. 1a shows additional diffraction peaks at 28.7° in BHE-NCM, which are indicative of secondary perovskite phases such as $CeNiO_3$,[30] La_4NiO_8,[31] and $LaCoMnO_6$.[32] These impurity phases are likely a result of phase segregation due to the larger ionic radii of La^{3+} and Ce^{3+} when incorporated into the bulk lattice of primary particles, leading to structural distortions and instability. In contrast, SHE-NCM samples effectively suppressed these impurity peaks, suggesting that surface-confined doping allows for more controlled incorporation of dopants without disrupting the core lattice structure.

Rietveld refinement (Fig. 1b, c and Table S1) further highlighted the structural advantages of SHE-NCM. The SHE-NCM exhibited a lower weighted profile R-factor (R_{wp}) of 6.16 and a higher intensity ratio of the planes (003) and (104) ($I(003)/I(104) = 2.21$). A higher $I(003)/I(104)$ ratio is associated with reduced cation mixing, particularly between Li^+ and Ni^{2+} ions, which is crucial for maintaining the layered structure and ensuring efficient lithium-ion diffusion. In contrast, BHE-NCM showed poorer refinement metrics, with a much higher R_{wp} and a lower $I(003)/I(104)$ ratio, indicating increased cation disorder and lattice strain due to heterogeneous dopant distribution.

Further analysis of single-doped samples revealed that NCM-Zr and NCM-Al maintained high phase purity without the presence of non-layered oxide phases, as evidenced by the absence of additional peaks in their XRD patterns. Conversely, NCM-La and NCM-Ce samples exhibited pronounced peaks at 28.7° (similar to those in BHE-NCM), corresponding to perovskite-type impurity phases. These peaks were much more prominent in BHE-NCM samples than in SHE-NCM, consistent with the refined XRD metrics, where the inferior structural integrity can be explained by lattice strain and defect formation associated with phase impurities.

High-resolution TEM imaging, combined with SEM (Fig. S1) and EDS mapping (Fig. 1d–m), reveals critical differences in dopant distribution and structural uniformity between the two designs. In BHE-NCM, dopants are integrated throughout the particle bulk during high-temperature calcination, leading to non-uniform elemental dispersion. Elemental mapping confirms irregular dopant localization, consistent with lattice strain observed via elongated (003) planes in HRTEM (Fig. 1e and f). This elongation is a structural fingerprint often associated with lattice distortion due to cation size mismatch and dopant-induced stress.[33] These localized distortions could be associated with the emergence of secondary perovskite-type peaks at 28.7° (111) in the XRD pattern, particularly in La- and Ce-rich samples, consistent with previous findings on perovskite segregation in Ni-rich layered oxides.[31] On the contrary, SHE-NCM exhibits a concentrated high-entropy dopant zone confined to the surface, with minimal penetration into the bulk. This design preserves the structural integrity of the core while limiting perovskite phase formation to the edges of the NCM secondary particles, as XRD analysis shows only a negligible signal of the perovskite phase, indicating better maintenance of the crystallographic framework.

This unique distribution of SHE-NCM is confirmed by depth-resolved XPS analysis in Fig. 2a–d, where Ce, La, Zr, and Al are concentrated at the surface and progressively diminish with etching. Core NCM components Ni and Li remain stable, suggesting minimal interdiffusion of dopants into the bulk. The rare-earth dopants Ce and Zr exhibit slight shifts in their binding energies (BE) compared to their oxide forms.[34,35] These shifts arise due to the incorporation into a high-entropy and

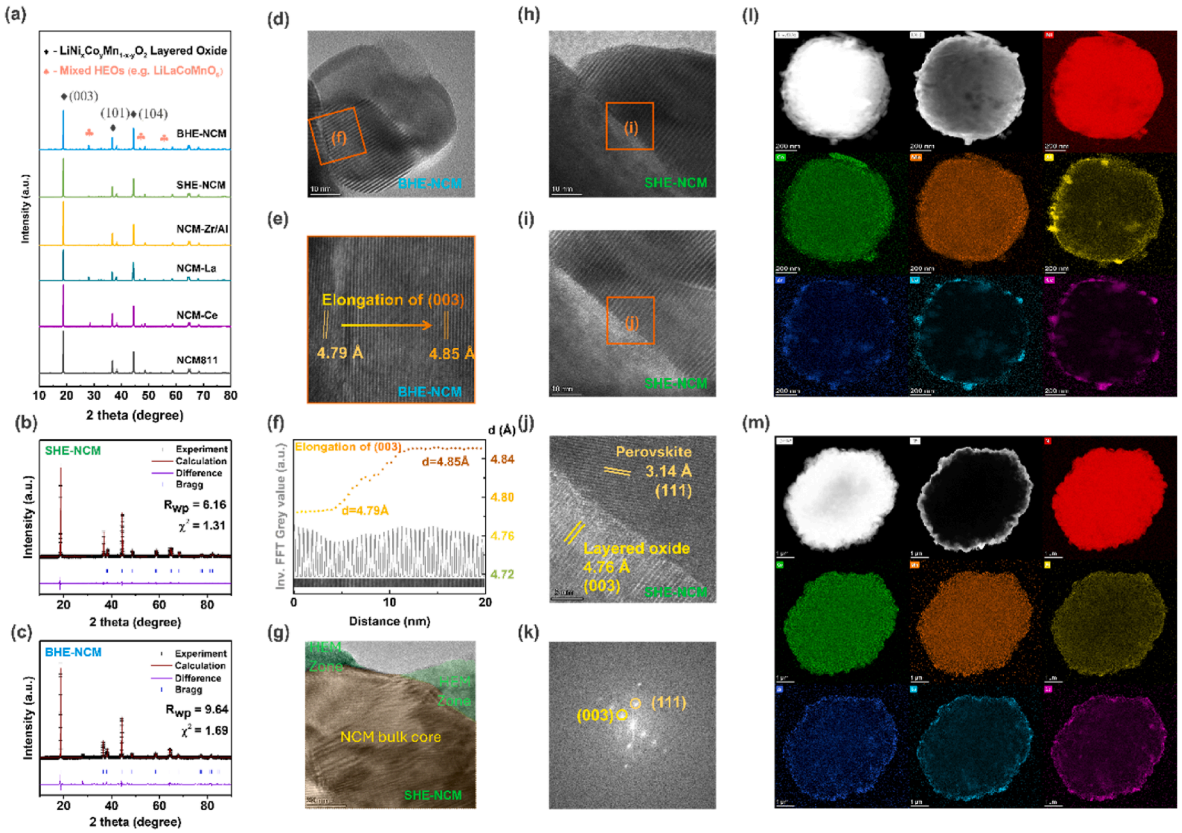

Fig. 1. (a) XRD pattern of BHE-, SHE-, Zr-, Al-, La-, and Al-doped NCM. XRD Rietveld refinement of (b) SHE-NCM and (c) BHE-NCM. TEM images of (d–e) BHE-NCM with (f) identification of elongated (003) plane (g) ranging from 4.79 A to 4.85 A and (h–j) SHE-NCM with (k) Fast Fourier transform (FFT) of (003)/(111) intersection. STEM-EDS elemental mapping of the different architectures of (l) BHE-NCM and (m) SHE-NCM.

multi-cation oxide lattice different from pure oxide phases, forming local structures such as $LiCeNiO_3$, $LiLaCoMnO_6$, etc. In particular, the BE observed in the Ce 3d spectrum is slightly lower (~0.4 eV) than typical values for CeO_2 (~882.0 and 888.0 eV for the Ce $3d_{5/2}$ multiplet). This downward shift suggests that Ce is not in the standard Fluorite structure of CeO_2, where it is 8-fold coordinated with oxygen, but rather in a distorted octahedral environment within the LiNCM lattice, likely in the form of $LiCeNiO_3$. Such structural changes are expected to alter Ce–O bond lengths and increase mixed-metal interactions (especially with Ni) and electron density, leading to a lower BE on the XPS spectra. Characteristics of La 3d also show a small difference relative to pure phase La_2O_3, where the BE gap of La $3d_{5/2}$ and $3d_{3/2}$ doublet is typically at 4.3 eV. The slightly smaller 4.2 eV gap can be explained by $LiLaCoMnO_6$-type configurations, as La is still bonded with oxygen but likely also surrounded by transition metals like Co and Mn. The shared oxygen coordination with other electronegative transition metals typically would alter the electron distribution and slightly increase the local electron density. In addition, the XANES spectra show that the Ni K-edge positions for SHE-NCM are nearly identical to those of the pristine P-NCM, indicating that the average Ni oxidation state in the bulk remains unchanged in SHE-NCM. The EXAFS spectra reveal that SHE-NCM maintains well-defined Ni–O and Ni–Ni coordination peaks similar to P-NCM, suggesting minimal disruption to the local bulk structure (Fig. S2). These findings provide strong evidence that the transition metal oxidation states and coordination environment within SHE-NCM's bulk are preserved, further confirming that the dopants in SHE-NCM are predominantly confined to the surface.

The Ni 2p XPS spectra of SHE-NCM reveal distinct features attributed to Ni^{2+} (854.6 eV) and Ni^{3+} (856.2 eV) oxidation states, with a distribution of Ni^{3+} (64.6%) and Ni^{2+} (35.4%) indicating a predominant presence of Ni in the higher oxidation state within the SHE-NCM surface structure (Fig. S3), largely influenced by the spatial localization of Zr dopants.[36] The higher ratio of Ni^{3+} is particularly important for maintaining the layered structure and preventing the transition to disordered phases during cycling. In the XPS depth profile, Zr 3d peaks (prominently around 181.8 eV, indicative of Zr^{4+}) were etched away much slowly than the rare earth element, which confirms the substitution of Zr into the transition metal (TM) sites or interstitial sites within the NCM lattice. The stable state Zr^{4+} and Al^{3+} are expected to reduce Li^+/Ni^{2+} mixing by segregating Ni and Li into their respective layers, owing to the similar ionic radius of Zr^{4+} (0.72 Å) to Li^+ (0.76 Å), and Al^{3+} (0.53 Å) to Ni^{2+} (0.55 Å), respectively. This is evident in Fig. 2a–c, where Ni^{3+} dominance in the Ni 2p and Ni 3p spectra is preserved during deeper etching cycles, suggesting better ordering of Ni and Li in separate planes. This stabilization effect limits the formation of rock-salt phases during cycling, which are commonly associated with the electrochemical degradation of NCM811 at high voltages.[2,37]

3.2. Analysis of thermal stability and lattice oxygen evolution

The thermal analysis of delithiated NCM samples (shown in Fig. 2e–g) reveals a cascade of exothermic phase transitions that signify critical structural changes: the layered-to-spinel and spinel-to-rock-salt transitions. For Pristine NCM, the layered-to-spinel shift appears to occur at 234.1 °C, while in BHE-NCM, this transition is observed at a slightly lower temperature of 221.4 °C, attributed to plane elongation and phase segregation (Fig. 1e and f) that promote structural rearrangement. In contrast, SHE-NCM exhibits a delayed transition at 258.7 °C, reflecting a noteworthy increase compared to BHE-NCM and P-NCM by 37.3 °C and 24.6 °C, respectively. This enhanced thermal resistance is linked to entropy stabilization within its surface-layered high-entropy zone, which effectively suppresses spinel phase

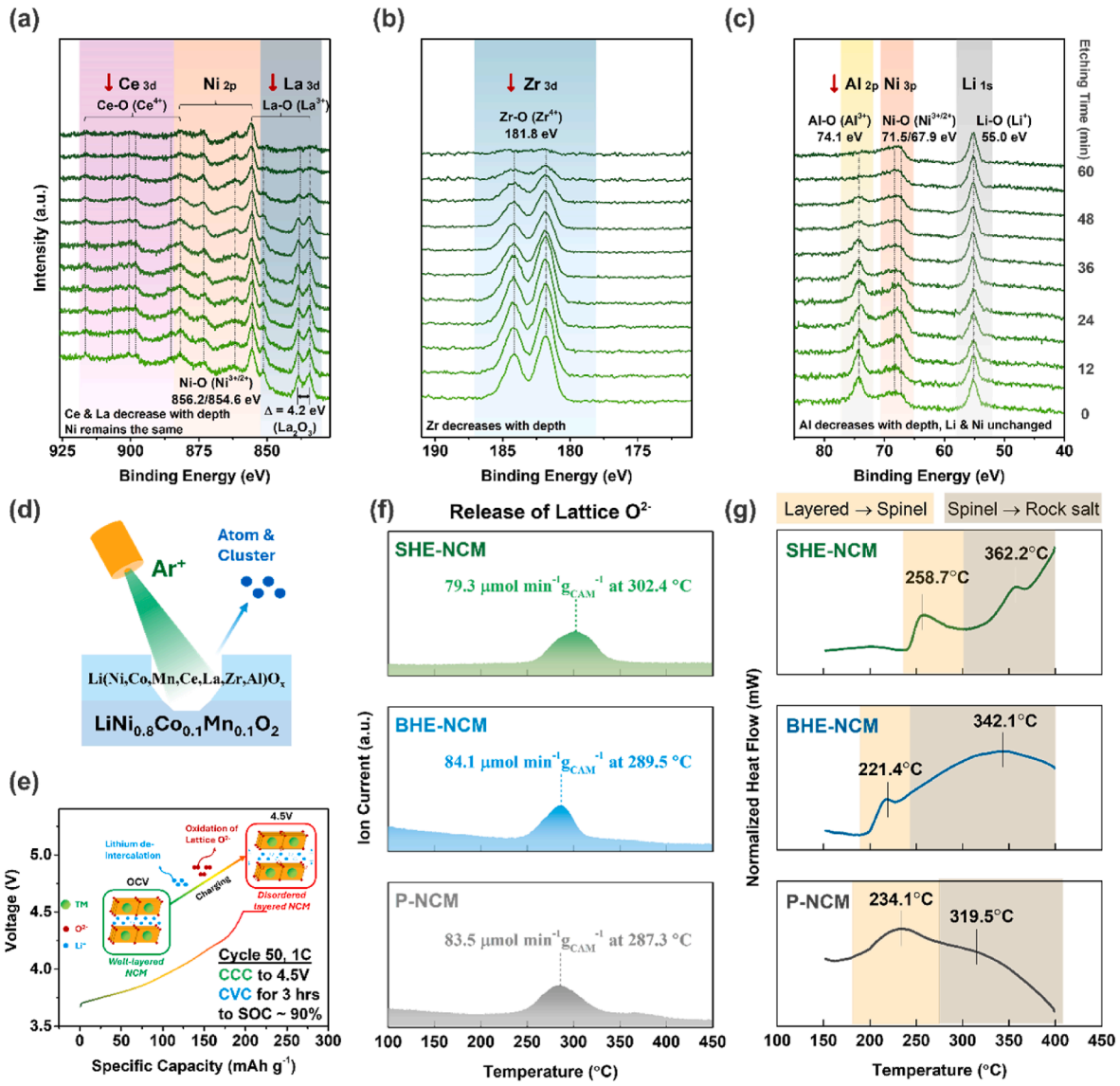

Fig. 2. XPS depth profiling of SHE-NCM, showing surface-to-sub-surface composition changes: (a) Ce 3d, Ni 2p, and La 3d spectra; (b) Zr 3d spectra; (c) Al 2p, Ni 2p, and Li 1s spectra; and (d) schematic illustration of Ar ion monoatomic sputtering depth profiling. (e) Specific capacity-voltage profile of battery charged up to 4.5 V for the de-lithiation induced lattice O^{2-} release. (f) Determination of temperature and rate of lattice oxygen release through TG-MS profile. (g) Determination of phase change temperature through TGA-DSC profile.

formation directly related to capacity degradation.[38]

It is important to recognize that the onset temperature determined from TGA-DSC analysis in Fig. 2g is not an absolute point of phase change but rather a useful indicator of when significant thermal degradation and phase transitions begin. While the layered-to-spinel transformation is partially reversible, the subsequent spinel-to-rock-salt phase change represents a permanent structural collapse that severely impedes lithium diffusion and long-term electrochemical performance.[39] For P-NCM, this critical transformation is observed at 319.5 °C, marking the onset of oxygen release and lattice breakdown. In BHE-NCM, this transition is delayed to 342.1 °C due to distributed dopant-induced strain relief and partial stabilization of the oxygen framework. However, SHE-NCM exhibits a notably higher onset temperature of 362.2 °C, indicating the most pronounced improvement in thermal robustness.

This superior behavior stems from the synergistic effects of multi-element entropy-assisted doping localized at the surface. The differential scanning calorimetry (DSC) curve of SHE-NCM reveals a smaller and broader exothermic peak compared to P-NCM, indicating a more gradual and less violent spinel-to-rock-salt transition. This behavior reflects the stabilizing influence of the entropy-rich surface layer, in which the dopants contribute to bond strengthening, defect suppression, and oxygen vacancy resistance. Specifically, Ce and La ions can form thermally stable oxide phases that buffer lattice oxygen loss through multivalent redox activity, while Zr^{4+} enhances Ni–O bond strength and inhibits cation migration.[19,39] Recent studies have shown that entropy-assisted surface phases can "pre-stabilize" the rocksalt or spinel framework, thereby moderating thermal transitions by reducing oxygen release kinetics and bond dissociation rates.[40]

As a result, the SHE-NCM cathode transitions more benignly, preventing the sharp exothermic events that typically accompany oxygen evolution in pristine NCMs. The exothermic peak shifts to higher temperatures, confirming that entropy-driven surface doping mitigates lattice collapse during thermal stress and enhances thermal safety under abuse conditions.

Mitigating the formation of the rock-salt phase and the associated oxygen evolution is crucial for ensuring the safety and extending the lifespan of Ni-rich lithium batteries. The enhanced thermal stability of

SHE-NCM can be further demonstrated through TGA-MS analysis, which measures the rate of lattice oxygen release from the delithiated cathode film. Fig. 2f shows that pristine NCM exhibits a maximum oxygen release at 287.3 °C with a peak rate of 83.5 μmol min^{-1} $g_{CAM}{}^{-1}$. Comparatively, BHE-NCM exhibits a similar onset at 289.5 °C with a rate of 84.1 μmol min^{-1} $g_{CAM}{}^{-1}$, but SHE-NCM significantly delays oxygen evolution to 302.4 °C and reduces the maximum release rate to 79.3 μmol min^{-1} $g_{CAM}{}^{-1}$. This shift reflects the suppression of oxygen vacancies and delayed phase transitions enabled by the strong metal-oxygen bonds introduced, linked to increased lattice energy and stronger M–O bonds (e.g., Zr–O ~766 ± 11 kJ mol^{-1} vs. Ni–O ~366 ± 30 kJ mol^{-1} [41,42]). The high-entropy surface enhances the resistance to oxygen vacancy formation by introducing disorder, which increases the oxygen vacancy formation energy. This thermodynamic barrier to lattice oxygen loss stabilizes the structure at elevated temperatures and under delithiation stress, thereby suppressing Li^{+}/Ni^{2+} cation disorder. XPS depth profiling of Zr 3d in Fig. 2b confirms the stable incorporation of Zr, with notable Zr 3d signals persisting even after deep etching cycles, reflecting its role in enhanced lattice cohesion under thermal stress.

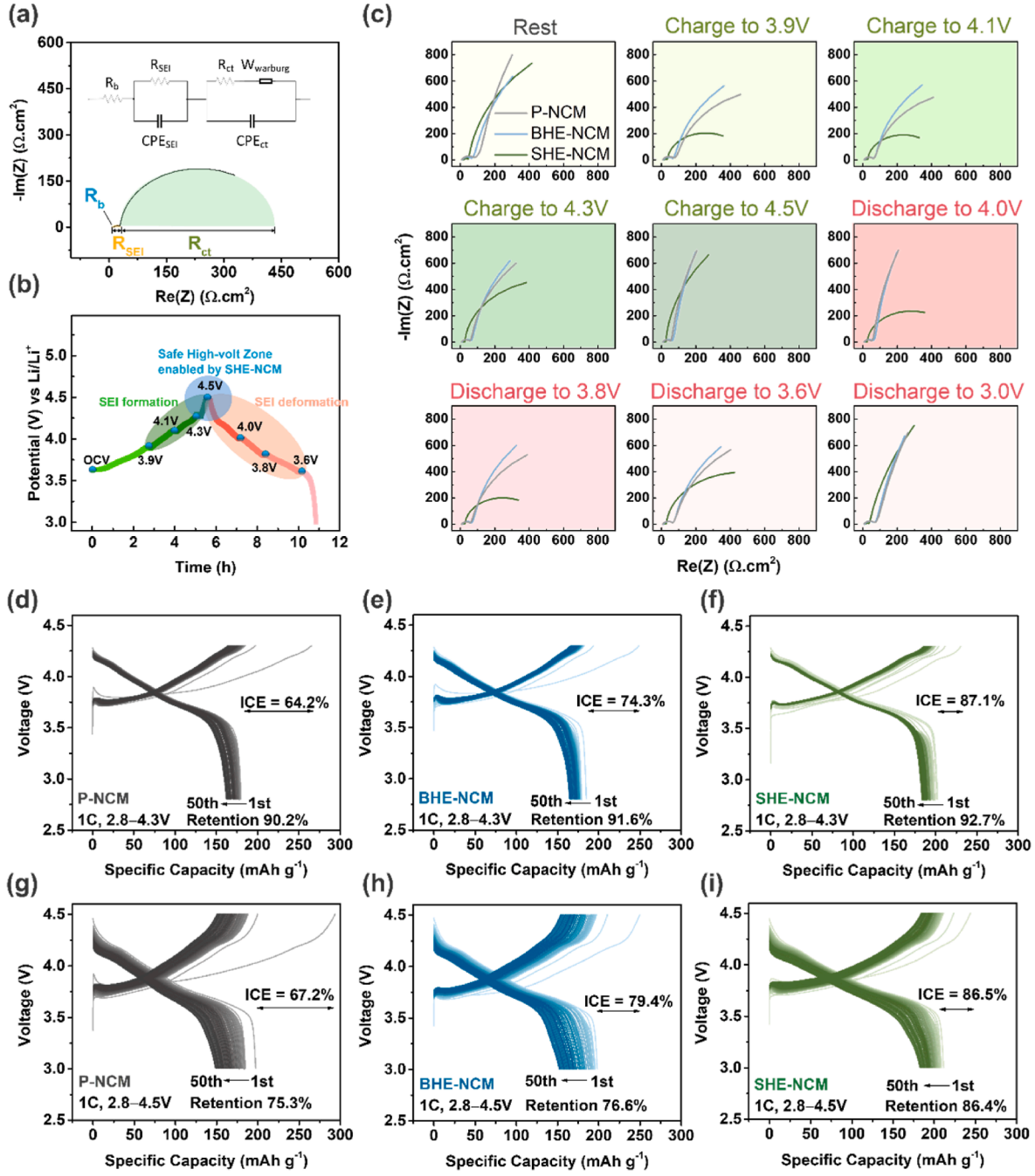

Fig. 3. (a) Experimental and fitted Nyquist plot using equivalent circuit model of the battery structure with distinct regions: bulk R_s, solid electrolyte interface R_{SEI} and charge transfer R_{ct}. (b) Voltage-dependent phase regions highlighting SEI formation and deformation across different voltage ranges 3.0 V–4.5 V. (c) EIS evolution for P-NCM, BHE-NCM, and SHE-NCM during the charging (3.9 V, 4.1 V, 4.3 V, 4.5 V) and discharging (4.0 V, 3.8 V, 3.6 V, 3.0 V) processes. Charge/discharge profiles at 1C with a cutoff voltage of 4.3 V for (d) P-NCM, (e) BHE-NCM, and (f) SHE-NCM, and at a cutoff voltage of 4.5 V for (g) P-NCM, (h) BHE-NCM, and (i) SHE-NCM.

3.3. Structure induced improvement on electrochemical performance

The structural enhancement of entropy-driven NCM is also assessed through a range of electrochemical characterizations. The electrochemical stability of entropy-driven NCM was first evaluated using SPEIS. The Nyquist plots (Fig. 3a) display the fitted equivalent circuit model, which consists of bulk resistance (R_s), solid electrolyte interface resistance (R_{SEI}), and charge transfer resistance (R_{ct}), each corresponding to specific electrochemical processes. The voltage-dependent phase regions (Fig. 3b) are used to highlight the dynamics of lithium diffusion during cycling. SHE-NCM, with the surface-entropy engineered zone, demonstrates a prominent reduction in R_{SEI} compared to both BHE-NCM and P-NCM. It was widely discussed that a reduced SEI impedance allows for faster Li-ion transport across the interface, minimizing polarization and voltage drops during electrochemical cycling, thus enabling faster charge and discharge cycles.[43–45] This can be attributed to the rare earth dopants Ce and La confined on the surface, providing chemical buffering and interfacial passivation through the formation of stable surface oxides, which mitigate oxygen evolution and side reactions at elevated voltages. Lower SEI resistance directly enhances rate performance (Fig. 4a–c). SHE-NCM exhibits superior capacity retention and voltage stability compared to P-NCM and BHE-NCM, especially at higher current densities, retaining 75% and 70% of its capacity at a 5C rate when cycled up to 4.3 V and 4.5 V, respectively. The rate capability of SHE-NCM showcases its robust ion transfer and minimal degradation under high current densities. Furthermore, SHE-NCM demonstrates stable recovery upon returning to 0.1C after high-rate testing at a higher voltage cutoff (2.8–4.5 V), indicating that the entropy-modified surface remains intact under extreme electrochemical stress without significant micro-cracking.[43]

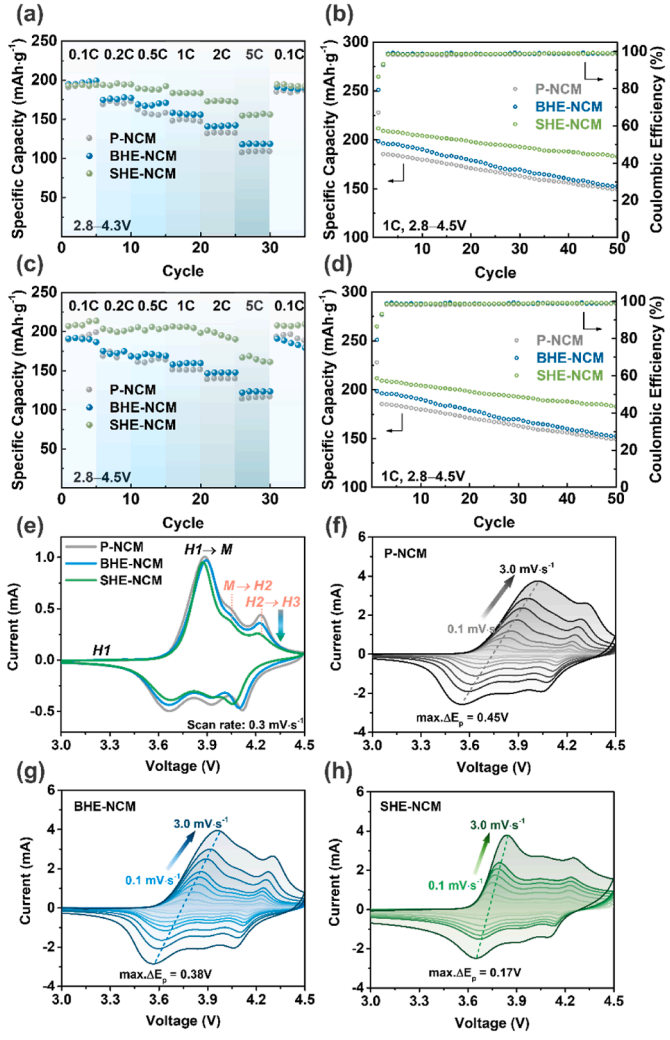

Fig. 4. Half-cell rate performance at 0.1C, 0.2C, 0.5C, 1.0C, 2.0C, 5.0C with cut-off voltage of (a) 4.3 V and (c) 4.5 V. Half-cell cycling performance with cut-off voltage of (b) 4.3 V and (d) 4.5 V. (e) Evaluation of reversibility of half-cell performance via cyclic voltammetry with current dependence on scan rate in (f) P-NCM, (g) BHE-NCM, and (h) SHE-NCM.

This improved interface stability minimizes electrolyte decomposition during high-voltage charging, effectively preserving the electrolyte-electrode contact and enhancing lithium-ion conductivity. Such behavior is particularly crucial during the transition to 4.3 V and 4.5 V, where high-voltage stress typically induces SEI thickening and surface degradation. This improved high-voltage stability is also evident from the cycling performance of SHE-NCM, with more stable voltage plateaus and higher capacity delivery when charged and discharged at different cut-off voltages (Fig. 3d–i and Tables S2 and S3).

In contrast, BHE-NCM exhibits impedance characteristics that are relatively unstable compared to SHE-NCM, similar to those of pristine NCM, with Nyquist plots showing larger *x*-axis intercepts at elevated voltages, reflecting increased charge transfer resistance (R_{ct}) during high-voltage charging. While the localized doping may introduce some extent of structure enforcement, it also introduces localized strain and phase segregation, accelerating interfacial degradation during cycling. Specifically, rare-earth dopants La and Ce contribute to lattice distortion and elongated planes, potentially exacerbating impedance growth over extended cycling. This is consistent with the result of thermal analyses, showing that high-entropy doping in localized bulk-like structure led to premature phase transitions and elevated oxygen evolution. This instability, particularly evident during charging beyond 4.1 V, points to poor electrochemical interface integrity caused by Ni/Li cation mixing and SEI degradation, promoting phase transitions into spinel and rock-salt structures. Post-cycling SEM images in Fig. 5a–c further reveal different degrees of microcrack formation and surface roughening upon delithiation of BHE-NCM and SHE-NCM. These structural and interfacial instabilities render BHE-NCM more vulnerable to capacity fade and electrolyte decomposition during high-voltage cycling, whereas the ability of SHE-NCM to sustain a low R_{ct} through both the charging and discharging sequence is indicative of a more resilient electrochemical interface that resists cracking and maintains lithium diffusion pathways. Further interpretation of the impedance behavior of these systems is beyond the scope of this paper.

The CV profile of SHE-NCM reveals significant improvement in redox behavior and phase transition dynamics, particularly during high-voltage cycling. The multi-step phase transitions of Ni-rich NCM cathodes, denoted as H1-M-H2-H3, are critical in dictating both the reversibility and stability of the cathode material. Especially, the H2-H3 transition was widely accepted as the onset of spinel-like and rock salt formation and considered the most irreversible.[38,39,46] As observed in Fig. 4e, SHE-NCM demonstrates significantly flattened redox peaks corresponding to the undesirable and irreversible M-H2 (from layered to distorted layered) and H2-H3 transitions. This phenomenon suggests a more uniform and controlled redox behavior within the system, potentially attributed to improved electrode-electrolyte interaction and enhanced charge transfer kinetics, as evidenced by SPEIS showing that SHE-NCM consistently achieves the lowest charge-transfer resistance (R_{ct}) during high-voltage cycling. This not only implies enhanced ion diffusion but also reflects a more robust surface structure that effectively minimizes irreversible phase transformations. The effect stems from surface segregation of large-radius rare-earth dopants (e.g., La and Ce) forming stable oxides, which passivate the interface and buffer lattice oxygen loss via their multivalent redox characteristics. The smooth current response observed between 4.3 V and 4.5 V in SHE-NCM further suggests mitigated lattice oxygen oxidation, consistent with TGA-MS data demonstrating significantly delayed and reduced oxygen evolution compared to its counterparts. The entropic stabilization provided by

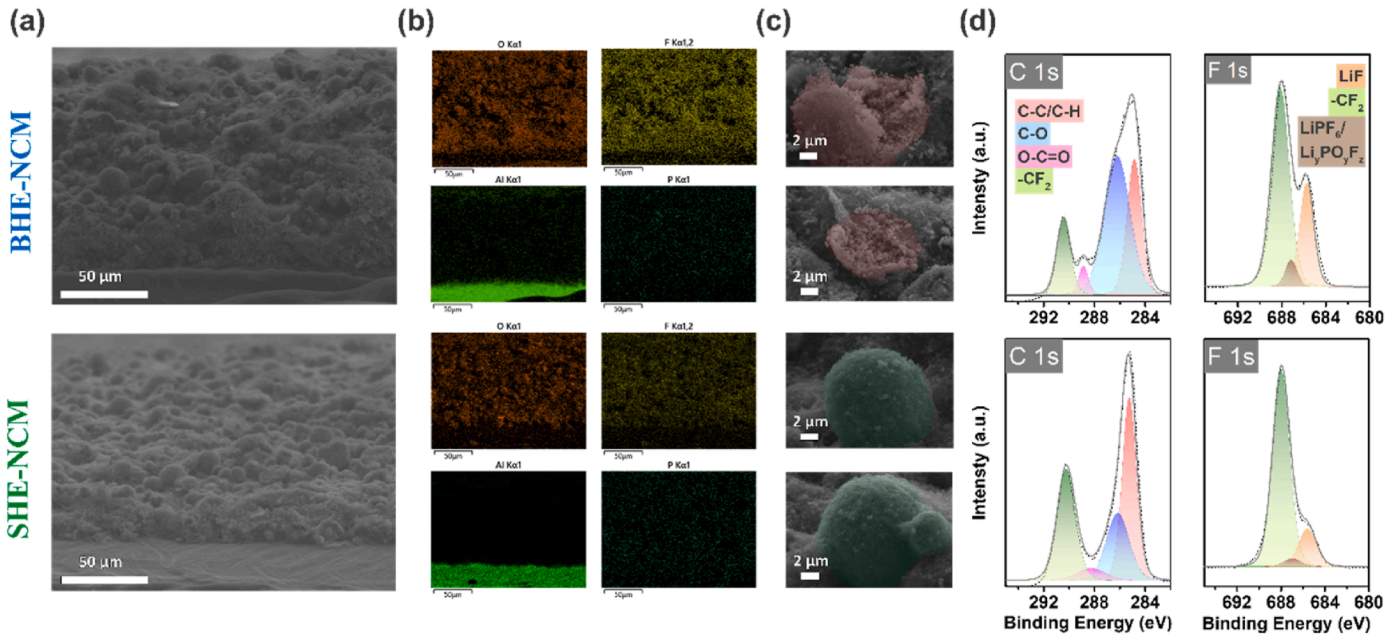

Fig. 5. Post-cycling characterization of BHE-NCM and SHE-NCM. (a) Cross-sectional SEM images of BHE-NCM and SHE-NCM electrodes after cycling with differences in surface morphology and crack formation. (b) Cross-sectional EDS mapping showing elemental distributions. (c) Top-view SEM images revealing secondary particle-level macro- and micro-cracks. (d) Surface XPS analysis of chemical composition changes post-cycling.

the high-entropy surface layer not only limits cation mixing but also restricts oxygen evolution, effectively alleviating oxygen-driven lattice expansion and cracking. A similar phenomenon was reported by several studies, where entropy-driven surface stabilization in multi-cation oxides reduces the electrochemical breakdown of the electrode-electrolyte interface, especially at elevated voltages.[11,12,47]

Furthermore, unlike P-NCM and BHE-NCM, which suffer from pronounced polarization at high scan rates, SHE-NCM maintains more symmetric redox peaks (Fig. 4f–h). SHE-NCM reported a better reaction kinetics with a smaller voltage hysteresis (ΔE_p) of 0.17 V compared to pristine NCM (0.45 V), when scanned at different scanning rates. This high voltage gap between forward and reverse scans of P-NCM is indicative of relatively severe electrode polarization and sluggish phase reversibility when a higher voltage change is applied. This is reflective of significant lattice distortion and irreversible phase transitions triggered by the oxidation of lattice oxygen, especially as the voltage approaches 4.5 V.[38,46] BHE-NCM, though slightly improved over P-NCM, still shows notable polarization effects (0.38 V) and peak broadening during cycling. This could be attributed to internal strain and phase segregation, as highlighted in its crystal structure, where the formation of perovskite secondary phases was observed from XRD and TEM. These features suggest that bulk-like localization introduces heterogeneity that partially mitigates but does not eliminate irreversible phase transitions.

Electrochemical cycling performance of SHE-NCM is also consistent with the improved electrode material reversibility. As shown in Fig. 4b–d, SHE-NCM maintains high initial coulombic efficiency (ICE = 87.1% at 4.3 V; 86.5% at 4.5 V) and excellent capacity retention over 50 cycles, outperforming BHE-NCM and pristine NCM under both cutoff conditions, and reflecting a stabilized electrochemical interface that resists degradation under both cycling fatigue and oxidative stress. The electrochemical cycling performance of single-doped NCM at a cutoff voltage of 4.5 V for single-doped NCM systems with La, Ce, Zr, and Al is also assessed to support the synergistic effect in SHE-NCM, which offers a more significant improvement in both capacity and cycle life (Table S4). In addition, the diffusion coefficients for BHE- and SHE-NCM cathodes before and after modification showed trivial differences to pristine NCM, indicating that the high-entropy material doping does not hinder lithium diffusion during extraction/insertion (Fig. S4 and Table S5).

3.4. Post-cycling characterization of chemo-mechanical structure

After cycling at high voltages (4.5 V), SHE-NCM and BHE-NCM electrodes exhibit distinct differences in their mechanical and chemical structures. In Fig. 5a–c, cross-sectional SEM and EDS analyses demonstrate that the BHE-NCM suffers from substantial degradation with the presence of micro- and macro-cracks, indicative of mechanical stress induced by volumetric changes during lithium insertion and extraction processes under high voltage. This structural deterioration is a major contributor to the increased charge-transfer resistance (R_{ct}) in Fig. 3c. The higher R_{ct} observed for BHE-NCM is characteristic of compromised charge-transfer kinetics and interfacial instability, partly due to the fractured surface with an increased exposure of electrode surface, accelerating electrolyte penetration, and inconsistent SEI formation. In contrast, SHE-NCM maintains smoother, intact post-cycling morphology due to entropy-engineered surface stabilization, which effectively suppresses phase transitions and structural collapse. The reduced R_{SEI} is just as critical for high-voltage cycling as it prevents polarization buildup, ensuring that lithium ions can effectively intercalate and de-intercalate without the impedance of thickened SEI layers.

This is further supported by TOF-SIMS depth profiling in Fig. 6, where SHE-NCM shows a rapid depletion of dissolved fragments of NCM such as LiF_2^- and NiF_3^-, contrary to the slower decay observed in BHE-NCM. In addition, the intensity of LiF_2^- and NiF_3^- increases sharply during the initial sputtering before reaching a maximum, which suggests that these dissolved species are primarily concentrated at the near-surface region of the CEI. SHE-NCM reaches its maximum intensity faster and with a sharper profile compared to BHE-NCM, implying a thinner, more uniform CEI layer where the dissolution is confined to the surface zone. This rapid removal of surface residues suggests that SHE-NCM maintains a more resilient surface structure during high-voltage operation, which limits the further formation of these parasitic species.[48] Furthermore, BHE-NCM exhibits a slower decay rate of C_2HO^- and PO_2^- species, representative of electrolyte and lithium conducting salt decomposition, suggesting a richer reservoir of electrolyte decomposition products trapped within its thicker CEI layer. 3D reconstructions and spatial distribution maps (Fig. 6e–f) align with this observation, revealing a thinner gradient concentration of interface

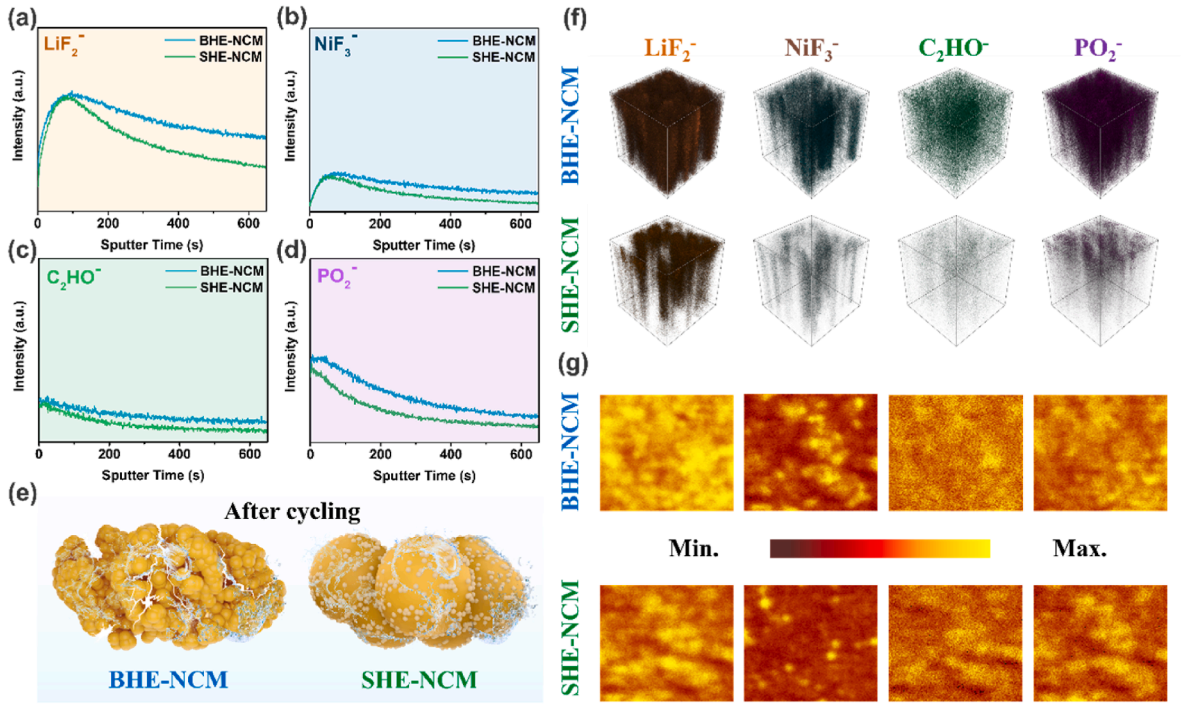

Fig. 6. Post-cycling ToF-SIMS depth profiles of (a) LiF_2^-, (b) NiF_3^-, (c) C_2HO^-, and (d) PO_2^- for BHE-NCM and SHE-NCM. (e) Schematic illustration of surface morphology changes after cycling. (f) 3D spatial distribution of electrolyte decomposition species and (g) corresponding surface intensity mappings.

degradation-generated species within SHE-NCM. This leads to reduced electrolyte decomposition reactions, less active material dissolution, with findings consistent with microscopic observations. This emphasizes the mitigation of performance degradation when SHE-NCM is cycled under high voltage, facilitated by its surface-entropy engineered structure.[44]

Surface XPS analysis complemented TOF-SIMS data by probing oxidation states and chemical composition of the post-reaction interlayer, since TOF-SIMS cannot resolve chemical bonding environments.[49] Fig. 5d shows that SHE-NCM exhibits fewer signs of electrolyte decomposition were observed with much weaker signals corresponding to C–O (287.2 eV), C=O (289.1 eV) and OCO_2 (290.2 eV) peaks compared to BHE-NCM. Furthermore, the F 1s spectra of SHE-NCM show a lower portion of LiF (685.5 eV) and $Li_xPO_yF_z$ (686.9 eV) components as compared to the C–F (687.9 eV) bonds, which is attributed to the PVDF binder on the electrode surface, indicative of suppressed electrolyte decomposition. This degradation mechanism aligns with the pronounced impedance rise observed in SPEIS measurements during prolonged cycling. The robust Zr and Al presence in SHE-NCM is believed to play a crucial role in enhancing the stability of the electrode-electrolyte interface and reducing Ni redox activity at the surface, thereby mitigating irreversible phase transitions like H2 to H3 that are commonly associated with structural collapse and the subsequent penetration of electrolyte into the structure.[50]

4. Conclusion

An entropy-assisted surface doping strategy was developed to stabilize Ni-rich NCM cathodes under aggressive high-voltage cycling by confining multi-element dopants within a high-entropy surface zone. This uniform surface dopant architecture effectively mitigates interfacial degradation and lattice instability, which typically accelerate during prolonged cycling and high-voltage operation. The entropy-driven structural modifications reduce Ni/Li disorder in the crystal lattice and inhibit spinel or rock-salt transformations, which allowed for the preservation of the layered structure. These improvements translate into higher capacity retention, lower interfacial resistance, and superior voltage stability compared to localized bulk-like counterparts. This dopant confinement is achieved through a stepwise doping strategy enabled by temperature-controlled synthesis, wherein multi-element incorporation is guided by differential thermal conditions to localize entropy at the surface. As confirmed by a series of material and electrochemical characterizations before and after cycling, the dopant-confined surface minimizes oxygen release, delays exothermic decomposition, and maintains a robust cathode-electrolyte interface. Enabled by a controlled synthesis route that facilitates multi-element incorporation through tailored thermal treatment, this strategy provides a robust and scalable surface-engineering platform for the development of next-generation high-voltage lithium-ion batteries.

CRediT authorship contribution statement

Leqi Zhao: Writing – original draft, Validation, Methodology, Investigation, Formal analysis, Data curation, Conceptualization. **Zezhou Lin:** Methodology, Conceptualization. **Yijun Zhong:** Methodology, Investigation, Formal analysis. **Hanwen Liu:** Formal analysis, Data curation. **Xiao Sun:** Formal analysis, Data curation. **Yu-Cheng Huang:** Data curation, Formal analysis. **William D.A. Rickard:** Resources, Formal analysis. **Tony Tang:** Resources, Project administration. **Zongping Shao:** Writing – review & editing, Supervision, Resources, Project administration, Funding acquisition, Conceptualization.

Declaration of competing interest

Zongping Shao is an Executive Editor for Materials Reports: Energy and was not involved in the editorial review or the decision to publish this article. The authors declare that they have no known competing financial interests or personal relationships that could have appeared to influence the work reported in this paper.

Acknowledgements

This work was supported by the Australian Research Council via Discovery Projects (Nos. DP200103315, DP200103332 and

DP230100685) and Linkage Projects (No. LP220200920). L. Zhao acknowledges the PhD scholarship supported by BLACKSTONE Minerals Ltd. The authors would like to acknowledge the John de Laeter Centre for the technical assistance of material characterizations, with additional support from the IONTOF M6 ToF-SIMS (funded by ARC LIEF, LE190100053) and the Kratos Axis Ultra XPS (ARC LIEF, LE120100026). The authors further acknowledge the support from the beamline staff at beamlines TPS 32A (TendeX-ray absorption spectroscopy beamline) at the National Synchrotron Radiation Research Center.

Appendix A. Supplementary data

Supplementary data to this article can be found online at https://doi.org/10.1016/j.matre.2025.100378.

References

1. Manthiram A. A reflection on lithium-ion battery cathode chemistry. *Nat Commun*. 2020;11(1):1550. https://doi.org/10.1038/s41467-020-15355-0.
2. Ryu HH, Namkoong B, Kim JH, Belharouak I, Yoon CS, Sun YK. Capacity fading mechanisms in Ni-Rich single-crystal NCM cathodes. *ACS Energy Lett*. 2021;6(8):2726–2734. https://doi.org/10.1021/acsenergylett.1c01089.
3. Yang H, Wu HH, Ge M, et al. Simultaneously dual modification of Ni-Rich layered oxide cathode for high-energy lithium-ion batteries. *Adv Funct Mater*. 2019;29(13):1808825. https://doi.org/10.1002/adfm.201808825.
4. Kim YJ, Rajagopal R, Kang S, Ryu KS. Novel dry deposition of $LiNbO_3$ or Li_2ZrO_3 on $LiNi_{0.6}Co_{0.2}Mn_{0.2}O_2$ for high performance all-solid-state lithium batteries. *Chem Eng J*. 2020;386:123975. https://doi.org/10.1016/j.cej.2019.123975.
5. Schipper F, Bouzaglo H, Dixit M, et al. From surface ZrO_2 coating to Bulk Zr doping by high temperature annealing of nickel-rich lithiated oxides and their enhanced electrochemical performance in lithium ion batteries. *Adv Energy Mater*. 2018;8(4):1701682. https://doi.org/10.1002/aenm.201701682.
6. Kong D, Hu J, Chen Z, et al. Ti-Gradient doping to stabilize layered surface structure for high performance High-Ni oxide cathode of Li-Ion battery. *Adv Energy Mater*. 2019;9(41):1901756. https://doi.org/10.1002/aenm.201901756.
7. Wang Y, Mi J, Wu ZS. Recent status and challenging perspective of high entropy oxides for chemical catalysis. *Chem Catal*. 2022;2(7):1624–1656. https://doi.org/10.1016/j.checat.2022.05.003.
8. Pan Y, Liu JX, Tu TZ, Wang W, Zhang GJ. High-entropy oxides for catalysis: a diamond in the rough. *Chem Eng J*. 2023;451:138659. https://doi.org/10.1016/j.cej.2022.138659.
9. Fu F, Liu X, Fu X, et al. Entropy and crystal-facet modulation of P2-type layered cathodes for long-lasting sodium-based batteries. *Nat Commun*. 2022;13(1):2826. https://doi.org/10.1038/s41467-022-30113-0.
10. Zhang R, Wang C, Zou P, et al. Compositionally complex doping for zero-strain zero-cobalt layered cathodes. *Nature*. 2022;610(7930):67–73. https://doi.org/10.1038/s41586-022-05115-z.
11. Tan X, Zhang Y, Xu S, et al. High-Entropy surface complex stabilized $LiCoO_2$ cathode. *Adv Energy Mater*. 2023;13(24):2300147. https://doi.org/10.1002/aenm.202300147.
12. Zhao C, Wang C, Liu X, et al. Suppressing strain propagation in ultrahigh-Ni cathodes during fast charging via epitaxial entropy-assisted coating. *Nat Energy*. 2024;9(3):345–356. https://doi.org/10.1038/s41560-024-01465-2.
13. Jung CH, Li Q, Kim DH, et al. Revisiting the role of Zr doping in Ni-rich layered cathodes for lithium-ion batteries. *J Mater Chem A*. 2021;9(32):17415–17424. https://doi.org/10.1039/D1TA04450H.
14. Huang J, Wang Y, Ling W, Yang X, Li Y, Zhou N. A synergistic modification of Zr doping and a lattice-reconstructed $La_2Li_{0.5}Ni_{0.5}O_4$ coating enables high-performance nickel-rich cathodes. *J Energy Storage*. 2025;106:114926. https://doi.org/10.1016/j.est.2024.114926.
15. Yang H, Li L, Liu C, et al. Simultaneous synthesis and synergetic stabilization of Zr-doped and $Li_6Zr_2O_7$-coated Ni-rich layered cathode for advanced lithium ion batteries. *Electrochim Acta*. 2020;364:137120. https://doi.org/10.1016/j.electacta.2020.137120.
16. Reissig F, Lange MA, Haneke L, et al. Synergistic effects of surface coating and bulk doping in Ni-Rich lithium nickel cobalt manganese oxide cathode materials for high-energy lithium ion batteries. *ChemSusChem*. 2022;15(4):e202102220. https://doi.org/10.1002/cssc.202102220.
17. Lv R, Wang C, Wang M. La-doped single-crystal Li-rich materials as high-capacity cathode materials for lithium-ion batteries. *Ionics*. 2025;11. https://doi.org/10.1007/s11581-025-06189-1. Published online March.
18. Ryu HH, Lee SB, Sun YK. Promoting grain growth in Ni-rich single-crystal cathodes for high-performance lithium-ion batteries through Ce doping. *J Solid State Electrochem*. 2022;26(9):2097–2105. https://doi.org/10.1007/s10008-022-05212-z.
19. Wang Z, Zhang J, Dong F, et al. Density functional theory guidance on rare earth doping—inhibition of lattice oxygen evolution in lithium-rich layered manganese oxide materials. *J Alloys Compd*. 2022;899:163311. https://doi.org/10.1016/j.jallcom.2021.163311.
20. Dai Z, Li Z, Chen R, Wu F, Li L. Defective oxygen inert phase stabilized high-voltage nickel-rich cathode for high-energy lithium-ion batteries. *Nat Commun*. 2023;14(1):8087. https://doi.org/10.1038/s41467-023-43792-0.
21. Jeong M, Kim H, Lee W, Ahn SJ, Lee E, Yoon WS. Stabilizing effects of Al-doping on Ni-rich $LiNi_{0.80}Co_{0.15}Mn_{0.05}O_2$ cathode for Li rechargeable batteries. *J Power Sources*. 2020;474:228592. https://doi.org/10.1016/j.jpowsour.2020.228592.
22. Cheng L, Zhang B, Su SL, Ming L, Zhao Y, Tan XX. Al-doping enables high stability of single-crystalline $LiNi_{0.7}Co_{0.1}Mn_{0.2}O_2$ lithium-ion cathodes at high voltage. *RSC Adv*. 2021;11(1):124–128. https://doi.org/10.1039/D0RA09813B.
23. Zhang Y, Liu J, Xu W, et al. Gradient doping Mg and Al to stabilize Ni-rich cathode materials for rechargeable lithium-ion batteries. *J Power Sources*. 2022;535:231445. https://doi.org/10.1016/j.jpowsour.2022.231445.
24. Wang Y, Chen C, Weng S, Li C, Xia Y, Lu X. Stabilizing ultra-high Ni layered cathodes for high-voltage operation through Al doping with synergistic Sn modification. *Chem Eng J*. 2025;514:163172. https://doi.org/10.1016/j.cej.2025.163172.
25. Zhao L, Zhong Y, Cao C, Tang T, Shao Z. Enhanced high-temperature cycling stability of garnet-based all solid-state lithium battery using a multi-functional catholyte buffer layer. *Nano-Micro Lett*. 2024;16(1):124. https://doi.org/10.1007/s40820-024-01358-9.
26. Li R, Huang Q, Wei K, Xia H. Quantitative analysis by thermogravimetry-mass spectrum analysis for reactions with evolved gases. *J Vis Exp*. 2018;140:58233. https://doi.org/10.3791/58233.
27. Randles JEB. Kinetics of rapid electrode reactions. *Discuss Faraday Soc*. 1947;1:11–19. https://doi.org/10.1039/DF9470100011.
28. Ševčík A. Oscillographic polarography with periodical triangular voltage. *Collect Czech Chem Commun*. 1948;13:349–377. https://doi.org/10.1135/cccc19480349.
29. Wu F, Dong J, Chen L, et al. High-Voltage and high-safety nickel-rich layered cathode enabled by a self-reconstructive Cathode/Electrolyte interphase layer. *Energy Storage Mater*. 2021;41:495–504. https://doi.org/10.1016/j.ensm.2021.06.018.
30. Harikrishnan MP, Bose AC. Porous $CeNiO_3$ with an enhanced electrochemical performance and prolonged cycle life (>50 000 cycles) via a lemon-assisted sol–gel autocombustion method. *New J Chem*. 2022;46(31):15118–15129. https://doi.org/10.1039/D2NJ02295H.
31. Zhang H, Qin L, Huang X, et al. Perovskite-coated small-size single-crystalline W-doped Ni-rich cathodes with greatly enhanced power density for Li-ion batteries. *J Mater Chem A*. 2024;12(36):24542–24548. https://doi.org/10.1039/D4TA04197F.
32. Ding B, Han C, Zheng L, Zhang J, Wang R, Tang Z. Tuning oxygen vacancy photoluminescence in monoclinic Y_2WO_6 by selectively occupying yttrium sites using lanthanum. *Sci Rep*. 2015;5(1):9443. https://doi.org/10.1038/srep09443.
33. Lin Z, Fan K, Liu T, et al. Mitigating lattice distortion of high-voltage $LiCoO_2$ via core-shell structure induced by cationic heterogeneous Co-Doping for lithium-ion batteries. *Nano-Micro Lett*. 2023;16(1):48. https://doi.org/10.1007/s40820-023-01269-1.
34. Moulder JF. Handbook of X-Ray Photoelectron spectroscopy: a reference book of standard Spectra for identification and interpretation of XPS data. *Physical Electronics Division, Perkin-Elmer Corporation*. 1992.
35. Gorham Justin. *NIST X-ray Photoelectron Spectroscopy Database - SRD 20*. 2012. https://doi.org/10.18434/T4T88K. Published online October 10.
36. Chen H, Hu Q, Huang Z, et al. Synthesis and electrochemical Study of Zr-Doped Li$[Li_{0.2}Mn_{0.54}Ni_{0.13}Co_{0.13}]O_2$ as cathode material for Li-Ion battery. *Ceram Int*. 2016;42(1, Part A):263–269. https://doi.org/10.1016/j.ceramint.2015.08.104.
37. Friedrich F, Strehle B, Freiberg ATS, et al. Editors' Choice—capacity fading mechanisms of NCM-811 cathodes in lithium-ion batteries studied by X-ray diffraction and other diagnostics. *J Electrochem Soc*. 2019;166(15):A3760. https://doi.org/10.1149/2.0821915jes.
38. Liu X, Xu GL, Kolluru VSC, et al. Origin and regulation of oxygen redox instability in high-voltage battery cathodes. *Nat Energy*. 2022;7(9):808–817. https://doi.org/10.1038/s41560-022-01036-3.
39. Jung SK, Kim H, Song SH, Lee S, Kim J, Kang K. Unveiling the role of transition-metal ions in the thermal degradation of Layered ni–co–mn cathodes for lithium rechargeable batteries. *Adv Funct Mater*. 2022;32(13):2108790. https://doi.org/10.1002/adfm.202108790.
40. Park K, Ham DJ, Park SY, et al. High-Ni cathode material improved with Zr for stable cycling of Li-ion rechargeable batteries. *RSC Adv*. 2020;10(45):26756–26764. https://doi.org/10.1039/D0RA01543A.
41. Luo YR. *Comprehensive Handbook of Chemical Bond Energies*. CRC Press; 2007. https://doi.org/10.1201/9781420007282.
42. Moltved KA, Kepp KP. The chemical bond between transition metals and oxygen: electronegativity, d-Orbital effects, and oxophilicity as descriptors of metal–oxygen interactions. *J Phys Chem C*. 2019;123(30):18432–18444. https://doi.org/10.1021/acs.jpcc.9b04317.
43. Verma P, Maire P, Novák P. A review of the features and analyses of the solid electrolyte interphase in Li-ion batteries. *Electrochim Acta*. 2010;55(22):6332–6341. https://doi.org/10.1016/j.electacta.2010.05.072.
44. Joshi T, Eom K, Yushin G, Fuller TF. Effects of dissolved transition metals on the electrochemical performance and SEI growth in lithium-ion batteries. *J Electrochem Soc*. 2014;161(12):A1915. https://doi.org/10.1149/2.0861412jes.

45. Wang A, Kadam S, Li H, Shi S, Qi Y. Review on modeling of the anode Solid Electrolyte Interphase (SEI) for lithium-ion batteries. *npj Comput Mater*. 2018;4(1): 1–26. https://doi.org/10.1038/s41524-018-0064-0.
46. Adamo JB, Manthiram A. Understanding the impact of composition on the H2–H3 phase transition in high-nickel cathodes. *ACS Appl Energy Mater*. 2025;8(4): 2200–2208. https://doi.org/10.1021/acsaem.4c02730.
47. Cai M, Dong Y, Xie M, et al. Stalling oxygen evolution in high-voltage cathodes by lanthurization. *Nat Energy*. 2023;8(2):159–168. https://doi.org/10.1038/s41560-022-01179-3.
48. Lin Z, Ying Y, Xu Z, et al. A multifunctional zeolite film enables stable high-voltage operation of a LiCoO2 cathode. *Energy Environ Sci*. 2025;18(1):334–346. https://doi.org/10.1039/D4EE04370G.
49. Lombardo T, Walther F, Kern C, et al. ToF-SIMS in battery research: advantages, limitations, and best practices. *J Vac Sci Technol A*. 2023;41(5):053207. https://doi.org/10.1116/6.0002850.
50. Bak SM, Hu E, Zhou Y, et al. Structural changes and thermal stability of charged LiNixMnyCozO2 cathode materials studied by combined in situ time-resolved XRD and Mass spectroscopy. *ACS Appl Mater Interfaces*. 2014;6(24):22594–22601. https://doi.org/10.1021/am506712c.

Leqi (Mark) Zhao is a Ph.D. candidate at the Curtin Centre for Advanced Energy Materials and Technologies (CAEMT), Curtin University. He holds a Bachelor of Chemical Engineering (Honours) and a Bachelor of Finance, both awarded by Monash University in 2021. His research focuses on advanced synthesis and scalable production of electrodes and electrode/electrolyte interfaces for lithium-ion and solid-state batteries. He also has a strong interest in interfacial characterization techniques for battery materials, particularly X-ray photoelectron spectroscopy (XPS), and currently serves as an XPS operator at the John de Laeter Centre at Curtin University.

Zongping Shao is a John Curtin Distinguished Professor at Curtin University. His primary research areas include solid oxide fuel cells (SOFCs), ceramic separation membranes, low-temperature oxygen and hydrogen catalysis, perovskite solar cells, lithium/sodium-ion batteries, supercapacitors, water treatment, and sensors. He received his Ph.D. from the Dalian Institute of Chemical Physics in 2000 and conducted post-doctoral research at CNRS, France and Caltech, USA. He has published over 800 SCI papers, including in Nature, Science, and Nature Energy, with more than 89,000 citations (h-index: 145). A Clarivate Highly Cited Researcher (2014, 2017–2024), he serves as Associate Editor of Energy & Fuels and Materials Reports: Energy, and on several editorial boards.